

# Amorphous metal-organic frameworks loaded on BiVO<sub>4</sub> photoanodes with unique internal metal-like structure for promoting photoelectrochemical water splitting

Weihao Bai <sup>a,1</sup>, Hao Li <sup>a,1</sup>, Gang Peng <sup>a</sup>, Jinnan Wang <sup>a,\*</sup>, Aimin Li <sup>a</sup>, Philippe François-Xavier Corvini <sup>b</sup>

<sup>a</sup> State Key Laboratory of Pollution Control and Resource Reuse & School of the Environment Nanjing University, Nanjing 210023, China

<sup>b</sup> School of Life Sciences, University of Applied Sciences and Arts Northwestern Switzerland, Basel 4132, Switzerland

## ARTICLE INFO

### Keywords:

Ferrocene based MOFs  
Amorphous MOFs  
BiVO<sub>4</sub> photoanodes  
photoelectrochemical water splitting  
Oxygen evolution co-catalysts (OECs)  
Strong metal-support interaction (SMSI)  
Coordinatively unsaturated Ni sites

## ABSTRACT

Although ferrocene (Fc) based Metal-Organic Frameworks (MOFs) can act as oxygen evolution co-catalysts (OECs) for improvement of catalytic reactivity, the poor conductivity and lack of highly active metal sites limit its further application in photoelectrochemical (PEC) water splitting. Herein, the amorphous NiFc-MOF was grafted on BiVO<sub>4</sub> photoanode (BiVO<sub>4</sub>@aNiFc-MOFs) for efficient PEC water splitting. This novel BiVO<sub>4</sub>@aNiFc-MOFs exhibits high current density of 4.34 mA cm<sup>-2</sup> at 1.23 V<sub>RHE</sub> and relative low onset potential of 0.223 V<sub>RHE</sub>. The subsequent characterizations demonstrate that Ni species with metal-like state in bulk of aNiFc-MOFs form strong metal-support interaction with BiVO<sub>4</sub>, thereby promoting the interfacial charge transfer. Moreover, the surface of aNiFc-MOFs is short-range ordered with abundant coordinatively unsaturated Ni sites, creating a more favorable pathway for oxygen evolution reaction from thermodynamics. This work provides a simple method to design photoanodes with efficient OECs of amorphous MOFs for feasible PEC water splitting application.

## 1. Introduction

Photoelectrochemical (PEC) hydrogen generation using solar energy is considered as the most promising strategy to solve the energy crisis [1, 2]. However, the four electron process of water oxidation is thermodynamically unfavorable, resulting in the oxygen evolution reaction (OER) being the rate-determining step [3]. Therefore, much attention was paid to developing efficient metal oxide/sulfide photoanode materials such as ZnO [4,5], TiO<sub>2</sub> [6,7],  $\alpha$ -Fe<sub>2</sub>O<sub>3</sub> [8,9], WO<sub>3</sub> [10], BiVO<sub>4</sub> [11,12] and CdS [13,14]. Among them, BiVO<sub>4</sub>-based photoanode with higher theoretical solar-to-hydrogen conversion efficiency (9.2%) and photocurrent (7.5 mA cm<sup>-2</sup> under standard AM 1.5 solar light irradiation) attracted significant interest in PEC water splitting reaction [15]. Unfortunately, due to the relatively low carrier mobility of 0.044 cm<sup>2</sup>·V<sup>-1</sup>·s<sup>-1</sup> and a short hole diffusion distance of 70 nm [16,17], severe photogenerated charges recombination occurred both in the bulk and on the surface of BiVO<sub>4</sub>. Additionally, the rate constant of OER of BiVO<sub>4</sub> calculated from transient absorption spectroscopy is approximately 1.4 s<sup>-1</sup> [18], indicating a sluggish water oxidation kinetics of pristine BiVO<sub>4</sub> photoanode.

These inherent defects lead to serious lower photocurrent density and efficiency than the theoretical values, thereby limiting its practical application.

To enhance the PEC water splitting activity of BiVO<sub>4</sub> photoanodes, construction of heterogeneous interface, crystalline engineering, hybrid atoms doping and OECs modification have been extensively investigated [19–26]. Among them, OECs can not only provide additional active sites to decrease the activation energy of OER but also passivate the surface states for suppressing charge recombination, which is considered as the most efficient strategy to improve the PEC water splitting activity. Although precious metal catalysts such as IrO<sub>2</sub> and RuO<sub>2</sub> shown satisfactory OER catalytic activity, high cost limited their widespread application [27]. Recently, MOFs constructed from transition metal ions/clusters coordinated with organic ligands could act as highly efficient OECs owing to ordered structures, uniform dispersion of active sites, periodic arrangement of atoms, and high tenability [28–31]. The transition-metal complex ferrocene (Fc) and its derivatives are sandwich like aromatic organometallic compounds, which are formed by combining two cyclopentadienes and one Fe<sup>2+</sup> via strong ‘cation-π’ and

\* Corresponding author.

E-mail address: [wjnnju@163.com](mailto:wjnnju@163.com) (J. Wang).

<sup>1</sup> First author: Weihao Bai and Hao Li contributed equally to this work.



' $\pi$ - $\pi'$  interactions. Attributing to remarkable molecular structural stability and redox activity, Fc-based MOFs are widely applied in the field of catalysis [32,33]. Nevertheless, on one hand, the primary building blocks of the structure comprise O- donor redox-inactive organic ligands, which inefficiently facilitate routes for charge transfer [34,35]. On the other hand, the Fe atoms in Fc serve as bridging units with unsatisfied catalytic activity, which limited the availability of metal sites capable of functioning as active centers in MOFs [36]. Thus, these Fc-based MOFs OEC still faced problems involving poor conductivity of MOF skeletons and lack of highly active metal sites.

Various methods including post-modifying metal/organic components [37] and introducing additional active sites into MOFs [38] have been developed to address these challenges. Current study demonstrated that amorphization of long-range ordered crystalline MOFs (c-MOFs) could lead to more active unsaturated sites, higher conductivity, and improved photoluminescence efficiency [39–41]. During the amorphization process, the charge density between defective sites and adjacent coordination atoms undergoes redistribution, optimizing the local electronic structure to promote charge transfer and redox kinetics of catalysis [42]. Thus, it inspires us to synthesize the amorphous Fc-based MOFs on the BiVO<sub>4</sub> photoanode as highly efficient OECs.

In this work, we have modulated the crystallinity of Fc-based MOFs coordinated with Ni (NiFc-MOFs) via simply varying the concentration of compositional units in precursors. The amorphous NiFc-MOFs (*a*NiFc-MOFs) loaded on the BiVO<sub>4</sub> photoanode (BiVO<sub>4</sub>@*a*NiFc-MOFs) exhibit the highest PEC water splitting activity. Structure characterizations indicated that the surface of *a*NiFc-MOFs are short-range ordered with abundant coordinatively unsaturated Ni sites. While, its internal atomic structure of Ni displays a metal-like state, which forms a strong metal-support interaction (SMSI) with the supporter semiconductor BiVO<sub>4</sub>. The following carrier kinetic characterizations and density functional theory (DFT) calculations demonstrated that such unique structure of BiVO<sub>4</sub>@*a*NiFc-MOFs with SMSI greatly facilitated the interfacial charge transfer and separation. Meanwhile, the BiVO<sub>4</sub>@*a*NiFc-MOFs with abundant coordinatively unsaturated Ni sites could provide additional open metal sites for OER, resulting in a more favorable pathway for adsorbing O adsorbates, especially for the rate-determining step of adsorbing \*OOH. Consequently, BiVO<sub>4</sub>@*a*NiFc-MOFs photoanode achieves an excellent photocurrent density of 4.34 mA cm<sup>-2</sup> at 1.23 V versus the RHE, which is 3.3 times higher than that of pristine BiVO<sub>4</sub> electrode (1.31 mA cm<sup>-2</sup>), while its onset potential (0.223 V) is 269 mV lower than that of BiVO<sub>4</sub> (0.492 V). Thus, this work provides a simple method to prepare efficient, stable, and cost-effective BiVO<sub>4</sub> based photoanodes with amorphous MOFs (*a*-MOFs) OECs.

## 2. Experimental section

### 2.1. Chemicals and materials

1,1'-ferrocene dicarboxylic acid [FcDA, 98.0%], acetone (C<sub>3</sub>H<sub>6</sub>O, AR) and vanadyl acetylacetone [VO(acac)<sub>2</sub>, 99.0%] were purchased from Shanghai Macklin Biochemical Co., Ltd. Potassium iodide (KI, 99.0%), p-benzoquinone (99.5%, HPLC), bismuthnitrate pentahydrate [Bi(NO<sub>3</sub>)<sub>3</sub>·5 H<sub>2</sub>O, 99.0%], dimethyl sulfoxide (DMSO, 99.8%), boric acid (H<sub>3</sub>BO<sub>3</sub>, 99.5%), sodium sulfite (Na<sub>2</sub>SO<sub>3</sub>, 98.0%), sodium hydroxide (NaOH, AR) were supplied by Shanghai Aladdin Biochemical Technology Co., Ltd. Ethanol (HPLC), N, N-dimethylformamide (DMF, ≥ 99.5%) were obtained from Sinopharm Chemical Reagent Co., Ltd. Concentrated nitric acid (HNO<sub>3</sub>, 68.0 wt%), potassium hydroxide (KOH, AR), nickel (II) chloride hexahydrate (NiCl<sub>2</sub>·6 H<sub>2</sub>O, AR) were supplied by Nanjing Chemical Reagent Co., Ltd. All chemicals need not be further purified during the whole experiment.

## 2.2. Preparation of BiVO<sub>4</sub>@*a*NiFc-MOFs photoanodes

### 2.2.1. Synthesis of BiVO<sub>4</sub> photoanodes

Before synthesizing, fluorine doped SnO<sub>2</sub> (FTO) conductive glass was ultrasonized in acetone, ethanol and deionized water for 30 min, respectively. The BiVO<sub>4</sub> photoanodes were fabricated by the electrochemical deposition method in a typical three-electrode cell [43]. Briefly, the BiOI electrodes were firstly prepared at the constant potential (-0.1 V vs. Ag/AgCl for 150 s) using Bi(NO<sub>3</sub>)<sub>3</sub>·5 H<sub>2</sub>O (40.0 mM) and KI (0.4 M) solution (pH 1.7). After thoroughly rinsing with deionized water and drying at room temperature, 100  $\mu$ L vanadium precursor solution [DMSO solution containing 0.2 M VO(acac)<sub>2</sub>] was dripped onto the BiOI electrodes. Then, the nanofilms were heated in muffle furnace for 2 h (450°C, ramping rate 2 °C/min). The obtained electrodes were immersed in NaOH solution (1.0 M) for 30 min to remove the V<sub>2</sub>O<sub>5</sub> on the surface of BiVO<sub>4</sub>.

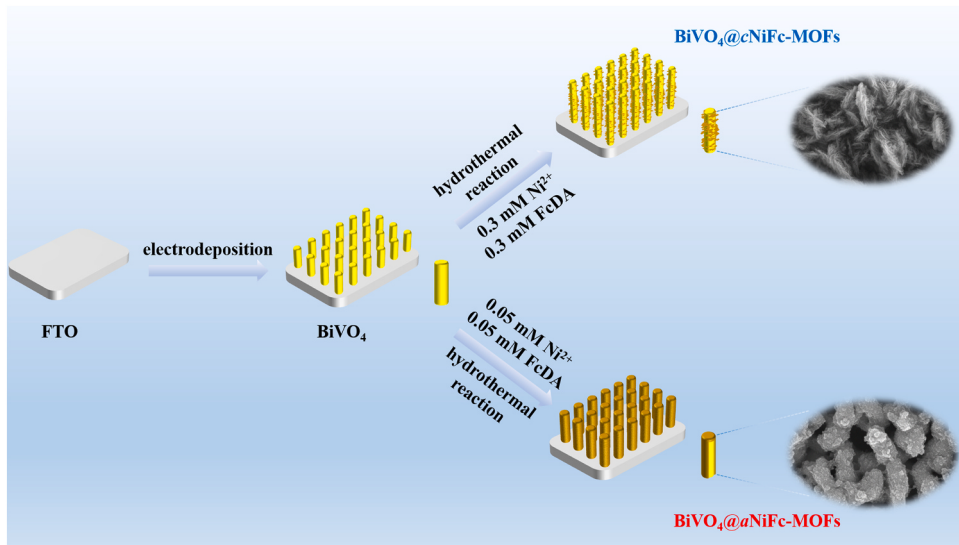
### 2.2.2. Synthesis of BiVO<sub>4</sub>@*a*NiFc-MOFs photoanodes

In this work, BiVO<sub>4</sub>@*a*NiFc-MOFs photoanodes were synthesized by a hydrothermal method. 0.05 mM FcDA was dissolved in 8 mL DMF, and then 4 mL 0.05 mM NiCl<sub>2</sub>·6 H<sub>2</sub>O aqueous solution was added in the mixture. After stirring for 10 min, the mixed solution was transferred into a 25 mL Teflon reactor with a piece of pre-fabricated BiVO<sub>4</sub> photoanode vertically submerged in it and heated at 125°C for 12 h. The obtained sample (BiVO<sub>4</sub>@*a*NiFc-MOFs) was rinsed with deionized water and dried in vacuum oven at 60°C for at least 12 h.

As comparisons, the crystalline NiFc-MOFs (cNiFc-MOFs) loaded on the BiVO<sub>4</sub> photoanode (BiVO<sub>4</sub>@cNiFc-MOFs) was also prepared. The preparation method of BiVO<sub>4</sub>@cNiFc-MOFs photoanodes was similar to that of BiVO<sub>4</sub>@*a*NiFc-MOFs mentioned above, except for that the concentration of FcDA and NiCl<sub>2</sub>·6 H<sub>2</sub>O solution was 0.3 mM.

## 2.3. Characterizations

The morphology and micro-structure of samples were observed by Scanning electron microscopy (SEM, Zeiss Sigma 300) and Transmission electron microscopy (TEM, FEI Talos F200X). Energy-dispersive X-ray spectra (EDS) was determined to analyze the elements distribution on photoanode surface by using Super-X (China). The content of each element of the catalysts loaded on FTO was quantified by Inductively coupled plasma mass spectrometry (ICP-MS). The crystallinity and crystal face of samples were identified by the X-ray diffractometer (XRD, Cu- $\kappa$  radiation, X'TRA, Switzerland) in the range of 10–70° (2 $\theta$ ) at a scanning rate of 5 min<sup>-1</sup>. Moreover, surface chemical composition and the valence states of elements were analyzed by X-ray photoelectron spectroscopy (XPS, PHI 5000 VersaProbe III with AES, ULVAC-PHI, Japan) using Al- $\kappa$  X-ray source, and all binding energies were calibrated by a C 1 s peak as standard (284.8 eV). The XPS argon-ion sputtering tests were performed with a practical sputter time of 30 seconds per cycle, totaling six cycles. The functional groups of samples were characterized by Fourier transform infrared spectrometer (FTIR, Thermo Scientific Nicolet iS20, America). The UV-vis diffuse reflectance spectra (UV-vis) was collected by the UV-vis spectrophotometer equipped with an integration sphere (UV-2600, Shimadzu, Japan) to evaluate the optical properties of photoanodes. The kinetics of electron separation and transfer were assessed by the steady-state Photoluminescence spectroscopy (PL) and Time-resolved photoluminescence spectroscopy (TRPL) with an excitation laser at 405 nm. Electron paramagnetic resonance (EPR) spectra of the photoanodes were recorded on Bruker EMX micro. The Ni K-edge X-ray absorption spectroscopy (XAS) experiments were performed and analyzed with the Athena and Artemis programs of the Demeter data analysis packages that utilizes the FEFF6 program to fit the EXAFS data.



**Scheme 1.** Schematic illustration of preparation process of  $\text{BiVO}_4@\text{cNiFc-MOFs}$  and  $\text{BiVO}_4@\text{aNiFc-MOFs}$ .

#### 2.4. Photoelectrochemical measurements

The PEC measurements of photoanodes were carried out by an electrochemical workstation (CHI700E, China) with a typical three-electrode configuration under illumination conditions (AM 1.5 G,  $100 \text{ mW cm}^{-2}$ ). An aqueous solution of 0.5 M potassium borate solution (KBi) electrolyte (pH 9.3) was used as the electrolyte.

Linear sweep voltammetry (LSV) was conducted at the scanning rate of 10 mV/s and the electrolyte was aerated with  $\text{N}_2$  for at least 30 min before the test. The incident photon-to-current conversion efficiency (IPCE) is determined by using the light source with a motorized monochromator. The stability test was carried out under 1.23 V vs. RHE. The hydrogen and oxygen were collected by Labsolar-6A system (Beijing Perfectlight), and the gas production was determined by gas chromatography (GC9790II, Fuli Instruments) every 20 min. The light-dark J-t test was conducted under 1.23 V vs. RHE and the shutter controller was set to switch every 30 s. Photoelectrochemical Impedance Spectroscopy (PEIS) was measured with a frequency range from  $10^{-1}$  to  $10^6 \text{ Hz}$  at  $0.2 \text{ V}_{\text{RHE}}$  (AM 1.5 G illumination). Mott-Schottky (M-S) plots were collected in the dark at a frequency of 1 kHz. Cyclic voltammetry (CV) measurements were carried out at scanning rate from 10 to 50 mV/s (potential range from 0.8 to 1.0  $\text{V}_{\text{RHE}}$ ). The electrochemical double layer capacitances ( $C_{dl}$ ) could be calculated by linear fitting of the current D-values under different scanning rates (half of the slope). Both charge separation efficiencies ( $\eta_{sep}$ ) and charge injection efficiencies ( $\eta_{inj}$ ) were identified by adding 0.2 M  $\text{Na}_2\text{SO}_3$  (holes scavenger) into KBi electrolyte.

The potential conversion formula of RHE and Ag/AgCl is as follows [44]:

$$E_{\text{RHE}} = E_{\text{Ag/AgCl}} + 0.0591 \times p\text{H} + E^\theta \quad (1)$$

Where  $E^\theta$  is the standard electrode potential of Ag/AgCl reference electrode at  $25^\circ\text{C}$  (0.1976 V),  $E_{\text{RHE}}$  refers to the converted potential vs. RHE and  $E_{\text{Ag/AgCl}}$  is the potential applied in a three-electrode system with Ag/AgCl as a reference electrode.

Incident photon to current conversion efficiency (IPCE) [45]:

$$\text{IPCE}(\%) = \frac{J_{ph} \times 1240}{P_{mono} \times \lambda} \quad (2)$$

Where  $J_{ph}$  is the measured photocurrent density ( $\text{mA}\cdot\text{cm}^{-2}$ ),  $P_{mono}$  is the power density of monochromatic light ( $\text{mW}\cdot\text{cm}^{-2}$ ),  $\lambda$  is the incident light wavelength (nm).

Applied bias photon to current efficiency (ABPE) [46]:

$$\text{ABPE} = J \times \frac{1.23 - V_b}{P_{light}} \quad (3)$$

where  $J$  is the LSV photocurrent density ( $\text{mA}\cdot\text{cm}^{-2}$ ),  $V_b$  is the applied voltage (V vs. RHE), and  $P_{light}$  is the intensity of incident light ( $100 \text{ mW}\cdot\text{cm}^{-2}$ , AM 1.5 G).

The Faradaic efficiency can be determined as [47]:

$$\eta_{O_2} = \frac{4F n_{O_2}}{Q} \quad (4)$$

$$\eta_{H_2} = \frac{2F n_{H_2}}{Q} \quad (5)$$

Where  $\eta_{O_2}$  and  $\eta_{H_2}$  is the Faraday efficiency,  $F$  is Faraday constant ( $96485 \text{ C}\cdot\text{mol}^{-1}$ ),  $n_{O_2}$  and  $n_{H_2}$  is the production of hydrogen and oxygen (mol),  $Q$  is the amount of charges generated by photocarriers (C).

The carrier concentration ( $N_d$ ) can be determined as [47]:

$$N_d = \frac{2}{e\epsilon_0\epsilon_r} \left( \frac{dC^{-2}}{dV} \right)^{-1} \quad (6)$$

Where  $N_d$  is carrier densities ( $\text{cm}^{-3}$ ),  $e$  is the electron charge ( $1.6 \times 10^{-19} \text{ C}$ ),  $\epsilon_0$  is vacuum dielectric constant ( $8.85 \times 10^{-14} \text{ F}\cdot\text{cm}^{-1}$ ),  $\epsilon_r$  is the relative dielectric constant of  $\text{BiVO}_4$  (68),  $\frac{dC^{-2}}{dV}$  is the slope of M-S plots ( $\text{F}^{-2}\cdot\text{cm}^2\cdot\text{V}^{-1}$ ).

The separation efficiencies of photo-generated electron ( $\eta_{sep}$ ) and hole pairs and surface charge injection efficiencies ( $\eta_{inj}$ ) can be determined as [46]:

$$\eta_{sep} = \frac{J_{\text{Na}_2\text{SO}_3}}{J_{\text{abs}}} \quad (7)$$

$$\eta_{inj} = \frac{J_{H_2\text{O}}}{J_{\text{Na}_2\text{SO}_3}} \quad (8)$$

Where  $J_{\text{abs}}$  is the photocurrent density ( $\text{mA}\cdot\text{cm}^{-2}$ ) when the percentage of absorbed photons to current is 100%,  $J_{\text{Na}_2\text{SO}_3}$  and  $J_{H_2\text{O}}$  are the photocurrent density ( $\text{mA}\cdot\text{cm}^{-2}$ ) for sulfite oxidation and water oxidation, respectively.

#### 2.5. DFT calculations

A simplified model of  $\text{aNiFc-MOFs}$  on the  $\text{BiVO}_4$  was constructed,

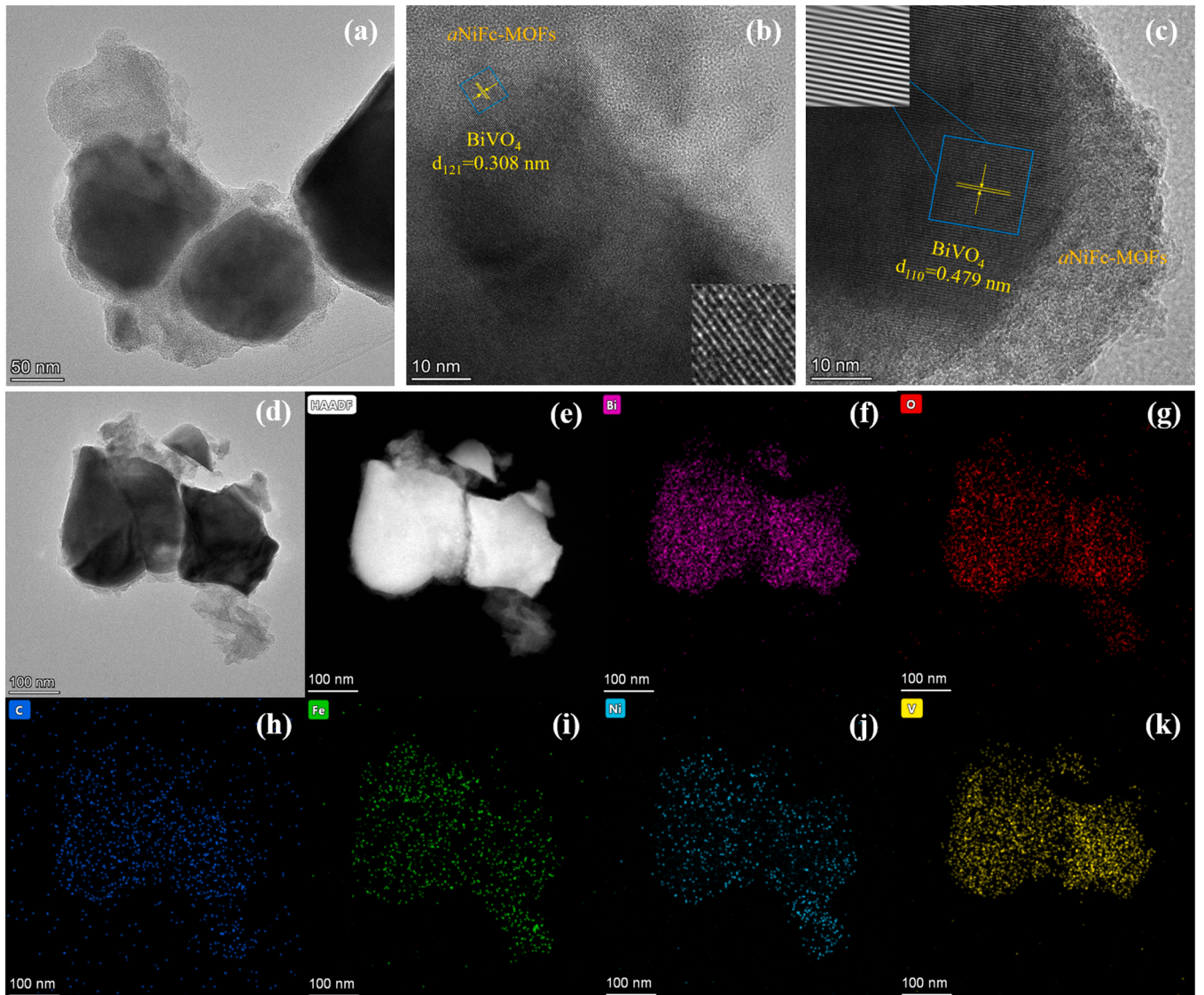


**Fig. 1.** (a)-(d) TEM images of  $\text{BiVO}_4@\text{aNiFc-MOFs}$  photoanode. (e) HADDF of  $\text{BiVO}_4@\text{aNiFc-MOFs}$  photoanode. EDS elemental mapping images of photoanode (f) Bi, (g) O, (h) C, (i) Fe, (j) Ni, (k) V.

which could directly gain insights into the role of  $\text{aNiFc-MOFs}$  with abundant coordinatively unsaturated Ni sites in mediating each step of OER process. The free energy associated with each step of the OER was calculated using density functional theory (DFT) within the Vienna Ab Initio Package (VASP). The PBE function within the generalized gradient approximation (GGA) method was employed to account for exchange-correlation effects. The projected augmented wave (PAW) method, with a plane wave expansion set and an energy cutoff of 500 eV, was utilized to incorporate core-valence interactions. Brillouin zone sampling was conducted with a  $3\times 3\times 1$  Monkhorst-Pack grid of k-points. To prevent periodic interactions, a vacuum layer extending 15 Å above the surface was introduced. The structural optimization iterated until electronic energy and force changes were both smaller than  $1.0\times 10^{-4}$  eV and  $0.02 \text{ eV } \text{\AA}^{-1}$ , respectively.

The Gibbs free energy change ( $\Delta G$ ) of each OER step was calculated using the following formula:

$$\Delta G = \Delta E + \Delta ZPE - T\Delta S \quad (9)$$

where  $\Delta E$  is the obtained electronic energy difference,  $\Delta ZPE$  is the zero-point energy difference,  $T$  is the temperature (298.15 K) and  $\Delta S$  is the entropy change. After frequency calculation, ZPE can be obtained

according to:

$$ZPE = \frac{1}{2} \sum h\nu_i \quad (10)$$

The TS values of adsorbed species can be calculated based on the vibrational frequencies by:

$$TS = k_B T \left[ \sum_k \ln \left( \frac{1}{1 - e^{-\frac{h\nu}{k_B T}}} \right) + \sum_k \frac{h\nu}{k_B T} \cdot \frac{1}{(e^{\frac{h\nu}{k_B T}} - 1)} + 1 \right] \quad (11)$$

### 3. Results and discussion

#### 3.1. Morphology and structure characterization of $\text{BiVO}_4@\text{aNiFc-MOFs}$ photoanode

The  $\text{BiVO}_4@\text{NiFc-MOFs}$  photoanodes were fabricated via a versatile method combining the electrodeposition and hydrothermal reaction (Scheme 1). The crystalline degree of NiFc-MOFs was modulated by simply controlling the concentration of compositional metal ion ( $\text{NiCl}_2 \cdot 6 \text{ H}_2\text{O}$ ) and organic linker (FcDA) precursors. Based on the analysis of crystalline-performance relationship (Text S1), amorphous NiFc-MOFs and crystalline NiFc-MOFs on  $\text{BiVO}_4$  photoanodes

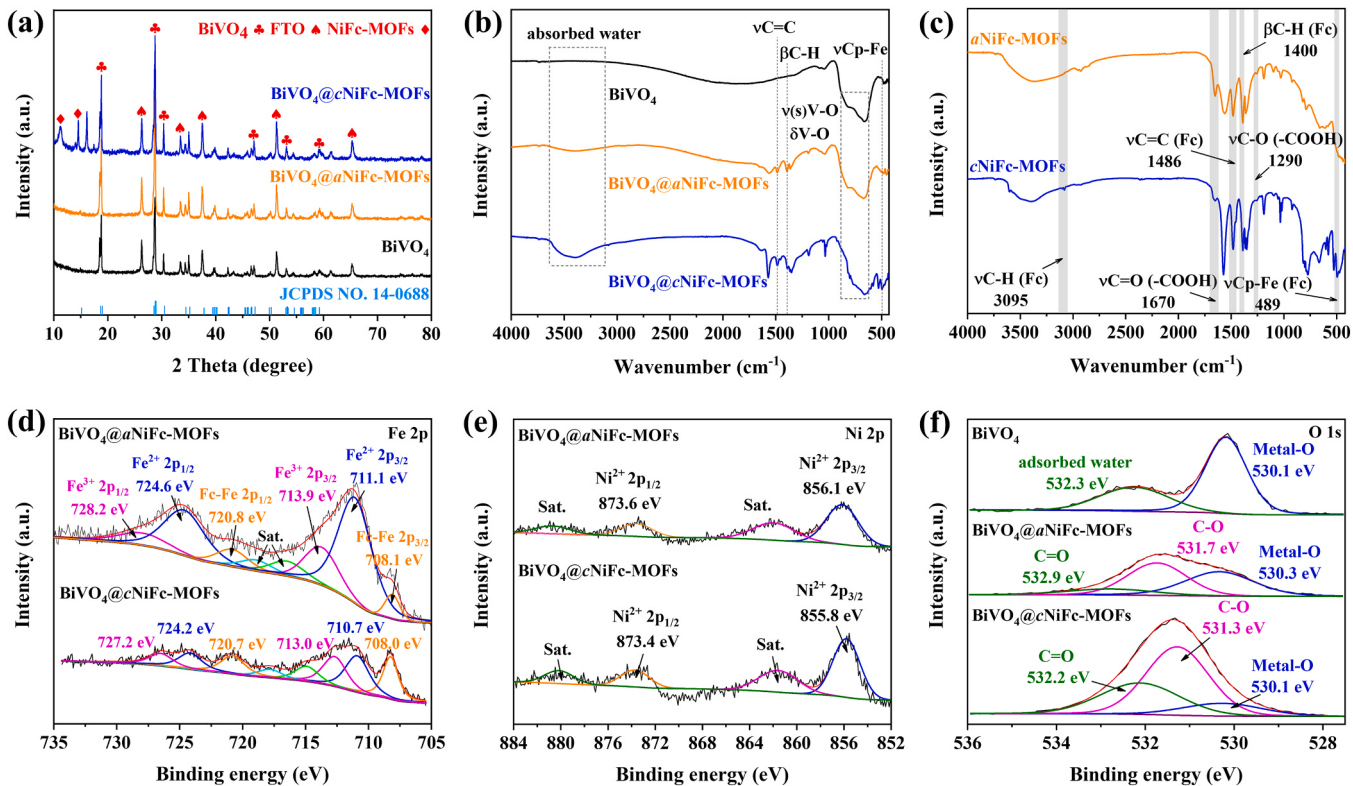


**Fig. 2.** (a) XRD patterns. FTIR spectra of (b)  $\text{BiVO}_4$ ,  $\text{BiVO}_4@\text{aNiFc-MOFs}$  and  $\text{BiVO}_4@\text{cNiFc-MOFs}$  photoanodes. (c) amorphous and crystalline NiFc-MOF powders. High-resolution XPS spectra of (d) Fe 2p, (e) Ni 2p and (f) O 1s.

( $\text{BiVO}_4@\text{aNiFc-MOFs}$  and  $\text{BiVO}_4@\text{cNiFc-MOFs}$ ) prepared with precursor (0.05 mM and 0.3 mM, respectively) are selected for further studies.

SEM image shows that loading of  $\text{aNiFc-MOFs}$  significantly increased the surface roughness of nanorods-like structured  $\text{BiVO}_4$  (Fig. S2a, b), while the  $\text{cNiFc-MOFs}$  vertically grown on the  $\text{BiVO}_4$  are dense and uniform nanosheets (Fig. S2c). Such morphology difference indicates that the  $\text{aNiFc-MOFs}$  are amorphously coated on the surface of  $\text{BiVO}_4$ . TEM images of  $\text{BiVO}_4@\text{aNiFc-MOFs}$  photoanode further confirm the amorphous structure of the NiFc-MOFs intimately coated on the surface of  $\text{BiVO}_4$ . The lattice fringes of 0.308 nm in Fig. 1b and 0.483 nm in Fig. 1c are corresponded to (121) and (110) plane of monoclinic  $\text{BiVO}_4$  [11], respectively. However, only a well coated  $\text{aNiFc-MOFs}$  layer on  $\text{BiVO}_4$  is evidently observed in all TEM images, with no obvious lattice fringes being visible (Fig. 1a-d). Moreover, the TEM-EDS (Fig. 1e-k) and SEM-EDS mappings (3) also indicate the uniform distribution of the  $\text{aNiFc-MOFs}$  on the surface of  $\text{BiVO}_4$ . The element contents of  $\text{BiVO}_4@\text{aNiFc-MOFs}$  photoanode are collected based on the TEM-EDS, SEM-EDS mappings and ICP-MS test (Fig. S3 and Table S1-2). The content of Ni in  $\text{BiVO}_4@\text{aNiFc-MOFs}$  is less than that of Fe (Ni:Fe  $\approx$  3:4), which is different from the typical atomic ratio of metal ion to Fe in Fc-based MOFs (1:1) [32,37], thereby indirectly proving the existence of Ni defects. In addition, compared with  $\text{BiVO}_4$  photoanode, the XRD peaks of the  $\text{BiVO}_4@\text{aNiFc-MOFs}$  are not changed obviously (Fig. 2a). Both of them agreed well with the standard card of monoclinic  $\text{BiVO}_4$  (JCPDS No.14-0688) [48]. However, two characteristic peaks of (400) and (001) plane of NiFc-MOFs were observed after loading of  $\text{cNiFc-MOFs}$  on  $\text{BiVO}_4$ . These results further confirmed the amorphous structure of the NiFc-MOFs on the surface of  $\text{BiVO}_4@\text{aNiFc-MOFs}$  photoanode.

The chemical composition and chemical state of samples are analyzed by using XPS and FTIR. The XPS survey spectra of  $\text{BiVO}_4@\text{aNiFc-MOFs}$  and  $\text{BiVO}_4@\text{cNiFc-MOFs}$  exhibit distinct characteristic peaks for the four elements (C, O, Fe, and Ni) (Fig. S4a). Meanwhile, the coated NiFc-MOFs mask the XPS signals from the underlying  $\text{BiVO}_4$ ,

leading to the absence of peaks corresponding to the Bi and V (Fig. S4b, c). However, the strong absorption peaks at 700–910  $\text{cm}^{-1}$  ascribed to deformation bending and symmetrical stretching vibration of V-O of  $\text{BiVO}_4$  [49,50] are shown in FTIR spectra for all samples (Fig. 2b). These experimental results indicate the successful synthesizing of  $\text{BiVO}_4$  substrate and uniform wrapping of the surface  $\text{aNiFc-MOFs}/\text{cNiFc-MOFs}$  layer. The bands at 489  $\text{cm}^{-1}$ , 1486  $\text{cm}^{-1}$  and 1400  $\text{cm}^{-1}$  (Fig. 2b) are respectively assigned to the stretching vibration of Cp-Fe (Cp = cyclopentadiene), C=C and the in-plane bending vibration of C-H in Fc ligand [32], suggesting the successful incorporation of Fc in  $\text{BiVO}_4@\text{aNiFc-MOFs}$ . XPS peaks of Fe 2p at 708.1 and 720.8 eV attributing to the divalent Fe ( $\text{Fe}^{2+} 2\text{p}_{3/2}$  and  $\text{Fe}^{2+} 2\text{p}_{1/2}$ ) in Fc units (Fig. 2d) can also confirm the successful introduction of Fc. The detailed FTIR bands assignments of NiFc-MOFs are marked in Fig. 2c. Notably, compared with the  $\text{aNiFc-MOFs}$ , band of C=O (1670  $\text{cm}^{-1}$ ) stretching vibration of the ferrocenedicarboxylic groups nearly disappeared in the  $\text{cNiFc-MOFs}$ , indicating that plenty of carboxyl groups of the Fc units were not coordinated to metal Ni sites in  $\text{aNiFc-MOFs}$  [36]. Thus, these Ni sites might be coordinatively unsaturated. The  $\text{Ni}2\text{p}_{3/2}$  (856.1 eV) and  $\text{Ni}2\text{p}_{1/2}$  (873.6 eV) peaks with satellite signals of  $\text{BiVO}_4@\text{aNiFc-MOFs}$  can be ascribed to divalent state Ni coordinated with oxygen atoms in ferrocene units (Fig. 2e). Analysis of O 1 s spectra (Fig. 2f) indicates the existence of Metal-O (530.3 eV), C-O (531.7 eV) and C=O (532.9 eV), further suggesting the successful coordination between  $\text{Ni}^{2+}$  and carboxylic group of ferrocene units. Moreover, compared with those of  $\text{BiVO}_4@\text{cNiFc-MOFs}$ , the XPS characteristic peaks of Ni 2p and O1s in  $\text{BiVO}_4@\text{aNiFc-MOFs}$  shifted towards the higher binding energy, also revealing the changes of surface Ni coordination environment [51,52]. Specifically, the amorphization of NiFc-MOFs on  $\text{BiVO}_4@\text{aNiFc-MOFs}$  photoanode led to the formation of abundant coordinatively unsaturated Ni centers with a higher valent state [37].

For deeper comprehension of the unsaturated coordination environment of Ni atoms, the atomic and electronic structure of the  $\text{BiVO}_4@\text{aNiFc-MOFs}$  photoanode was investigated by EPR, the Ni K-

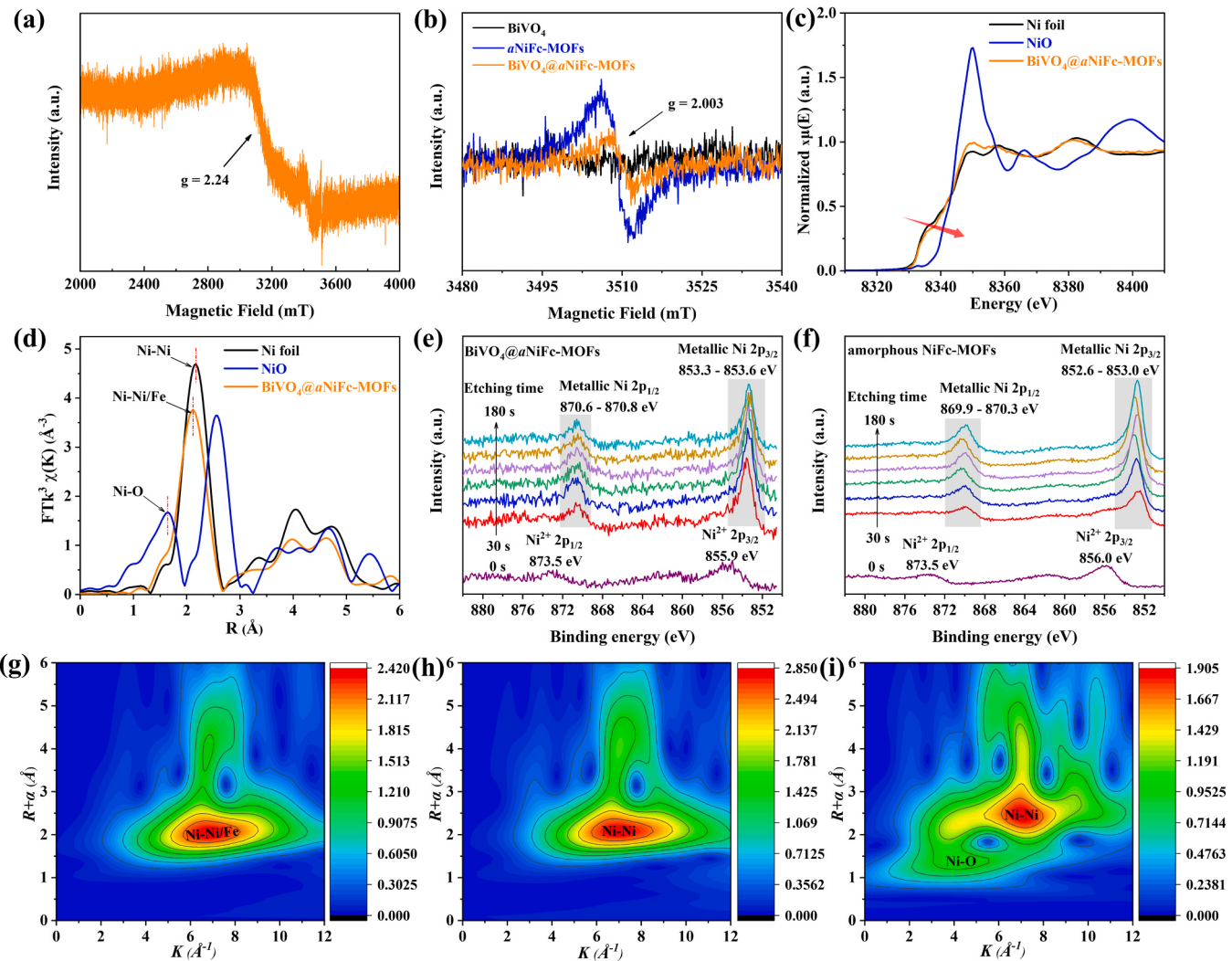


**Fig. 3.** (a)-(b) The EPR spectra of samples. (c) Ni K-edge XANES and (d) Fourier-transform EXAFS spectra of BiVO<sub>4</sub>@aNiFc-MOFs and reference samples. XPS argon-ion sputtering of (e) BiVO<sub>4</sub>@aNiFc-MOFs and (f) amorphous NiFc-MOF powders. The WT contour plots of (g) BiVO<sub>4</sub>@aNiFc-MOFs, (h) Ni foil and (i) NiO.

edge X-ray absorption near-edge structure (XANES), the extended X-ray absorption fine structure (EXAFS) and XPS argon-ion sputtering measurements. The EPR spectra of BiVO<sub>4</sub>@aNiFc-MOFs in Fig. 3a, b shows a strong signal at  $g = 2.24$  and 2.003, which respectively correspond to Ni cationic vacancies ( $V_{\text{Ni}}$ ) and O anion vacancies ( $V_{\text{O}}$ ) [53]. Notably, compared with the extremely strong  $V_{\text{O}}$  signal of pristine BiVO<sub>4</sub>, weak  $V_{\text{O}}$  signal of pristine BiVO<sub>4</sub> could be almost negligible, suggesting that most of  $V_{\text{O}}$  was generated in aNiFc-MOFs. The rich existence of cationic and anion vacancy defects in the aNiFc-MOFs could facilitate forming plenty of coordinatively unsaturated Ni sites, thereby greatly enhancing the surface water oxidation kinetics of the photocatalyst. Moreover, the analysis of EXAFS curve fitting reveals that the average coordination number (CN) of Ni-O in BiVO<sub>4</sub>@aNiFc-MOFs is  $1.1 \pm 0.1$  and the average CN of Ni-Ni is  $10.7 \pm 0.2$  (Fig. S5 and Table S3). Typically, the perfect cNiFc-MOFs exhibited a CN around 6 of Ni-O [32, 37, 54], further confirming the formation of abundant coordinatively unsaturated Ni sites in BiVO<sub>4</sub>@aNiFc-MOFs. Surprisingly, the Ni K-edge XANES spectra of BiVO<sub>4</sub>@aNiFc-MOFs display the absorption edge position similar to Ni foil, suggesting the valence state of the Ni species in bulk is close to 0 (Fig. 3c). Meanwhile, the relevant Ni EXAFS spectra of both Ni foil and BiVO<sub>4</sub>@aNiFc-MOFs show a prominent peak around  $2.1 \text{ \AA}$  (Fig. 3d), consistent with the lengths of the second coordination Ni-Ni/Fe shell, which is confirmed by the wavelet transform (WT) results (Fig. 3g-i). These XAS conclusions demonstrate that the Ni species

in BiVO<sub>4</sub>@aNiFc-MOFs retained the metal-like state, which was different from the surface chemical state results obtained from the high-resolution XPS spectra of Ni 2p.

Given that the limited depth of characterization (1–10 nm) achievable by XPS on the surface of the sample, the XPS argon-ion sputtering test was conducted to further investigate the elemental chemical state both on the surface and in the bulk of BiVO<sub>4</sub>@aNiFc-MOFs (Fig. 3e, f). Consistent with the XPS spectra of Ni 2p, the element Ni on the surface of both BiVO<sub>4</sub>@aNiFc-MOFs photoanode and amorphous NiFc-MOF powders were attributed to the divalent Ni before argon-ion etching. As the etching time increases, the XPS characteristic peaks of Ni<sup>2+</sup> diminished, and concomitantly, the characteristic peaks corresponding to metallic Ni became the dominant. This result confirmed that the Ni species in the bulk of aNiFc-MOFs loaded on the BiVO<sub>4</sub>@aNiFc-MOFs photoanode were metallic Ni. To eliminate potential systematic errors during the test, XPS sputtering measurements are conducted on the BiVO<sub>4</sub>@cNiFc-MOFs photoanode (Fig. S6a). The Ni 2p spectra was not changed within the etching process, suggesting that argon-ion etching had little impact on the oxidation state of Ni. Notably, the overall binding energies of metallic Ni 2p in BiVO<sub>4</sub>@aNiFc-MOFs were higher than those of aNiFc-MOFs. This observation suggested the presence of a distinctive chemical interaction between the metallic Ni in the bulk of aNiFc-MOFs and the supporting BiVO<sub>4</sub> semiconductor. Considering that the internal structure of BiVO<sub>4</sub>@cNiFc-MOFs was very similar to the typical supported

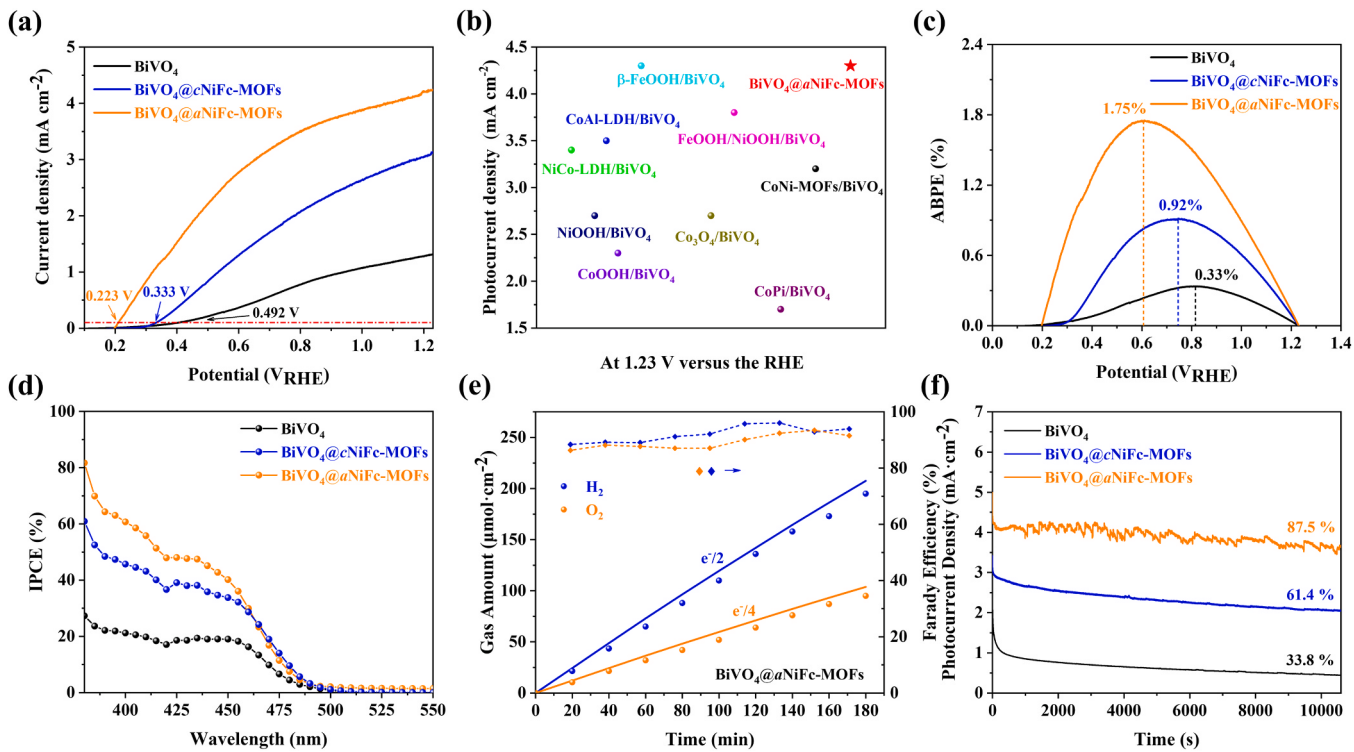


**Fig. 4.** (a) LSV. (b) Comparison of our photoanode with other common co-catalyst/ $\text{BiVO}_4$  photoanodes. (c) ABPE and (d) IPCE of  $\text{BiVO}_4$ ,  $\text{BiVO}_4@c\text{NiFc-MOFs}$  and  $\text{BiVO}_4@a\text{NiFc-MOFs}$  photoanodes. (e)  $\text{H}_2$  and  $\text{O}_2$  production at 1.23 V vs. RHE within 180 min and Faraday efficiencies for OER, HER. (f) Stability test at 1.23 V vs. RHE.

metal photocatalyst reported recently [55], such interaction might be the SMSI which could efficiently promote the interface charge. In addition, the XPS sputtering analysis of Fe 2p for the  $\text{BiVO}_4@a\text{NiFc-MOFs}$  photoanode and  $a\text{NiFc-MOFs}$  (Fig. S6b, c) reveals that the valence state of Fe element (notably the  $\text{Fe}-\text{Fe}^{2+}$ ) both in bulk and surface are almost the same.

Based on the above structure characterizations of samples, it could be concluded that the  $a\text{NiFc-MOFs}$  on  $\text{BiVO}_4@a\text{NiFc-MOFs}$  photoanode were actually short-range ordered with the complicated local atomic environment. Specifically, the surface structure of the  $\text{BiVO}_4@a\text{NiFc-MOFs}$  photoanode comprised a layer of NiFc-MOFs with abundant coordinatively unsaturated Ni sites, where the number of coordinated oxygen atoms (arising from the pair of carboxylate groups on each Fc unit) for Ni was less than six [32]. Nevertheless, its internal atomic structure underwent collapse during this distinctive growth process of MOF crystals. Local distortions in the  $a\text{NiFc-MOFs}$  resulted in bond breakages within the framework, consequently causing the Ni species in  $\text{BiVO}_4@a\text{NiFc-MOFs}$  to adopt a metal-like state. Therefore, due to the unique surface and internal structure,  $\text{BiVO}_4@a\text{NiFc-MOFs}$  photoanode had the potential to deliver a satisfactory PEC water splitting performance.

### 3.2. Photoelectrochemical water splitting performance

The PEC water splitting performance of all samples were studied under the simulated sun irradiation ( $100 \text{ mW}\cdot\text{cm}^{-2}$ ) in  $0.5 \text{ M KBr}$  electrolyte. As expected,  $\text{BiVO}_4@a\text{NiFc-MOFs}$  ( $4.34 \text{ mA cm}^{-2}$ ) achieves the highest photocurrent densities at 1.23 V<sub>RHE</sub> among these samples [ $\text{BiVO}_4@c\text{NiFc-MOFs}$  ( $3.13 \text{ mA cm}^{-2}$ );  $\text{BiVO}_4$  ( $1.31 \text{ mA cm}^{-2}$ )], and even superior to other common co-catalyst/ $\text{BiVO}_4$  photoanodes reported in previous literatures (Fig. 4a, b) [48,56–64]. Meanwhile, the onset potential of  $\text{BiVO}_4@a\text{NiFc-MOFs}$  (0.223 V<sub>RHE</sub>) can be obtained according to LSV curves (potential at the current density of  $0.1 \text{ mA cm}^{-2}$ ) [65], which displays the cathodic shifts of 110 mV and

269 mV compared with  $\text{BiVO}_4@c\text{NiFc-MOFs}$  and  $\text{BiVO}_4$  (Fig. 4a), respectively. The ABPE representing solar energy conversion efficiency was determined by subtracting the contribution of bias voltage. This metric could be calculated based on the data extracted from LSV curves.  $\text{BiVO}_4@a\text{NiFc-MOFs}$  photoanode exhibits a maximum ABPE of 1.75% at a relatively low bias of 0.61 V<sub>RHE</sub> (Fig. 4c). This value is approximately 1.9 times higher than the ABPE of  $\text{BiVO}_4@c\text{NiFc-MOFs}$ , recorded at 0.92% with a bias of 0.75 V<sub>RHE</sub>, and 5.3 times higher than the ABPE of the  $\text{BiVO}_4$ , which is 0.33% at 0.81 V<sub>RHE</sub>. It is noteworthy that the bias applied to achieve the peak ABPE aligns with the corresponding shifts in onset potentials. Moreover, the  $\text{BiVO}_4@a\text{NiFc-MOFs}$  photoanode exhibits the highest IPCE among all the samples, spanning the entire wavelength range from 400 to 550 nm (Fig. 4d). In the quantitative gas test, the yields of hydrogen and oxygen are respectively determined to be  $195.5$  and  $97.7 \mu\text{mol}$  after a 180-minute duration, with corresponding Faradaic efficiencies of 92.1% for hydrogen and 89.3% for oxygen (Fig. 4e). Such significant improvements of PEC performance highlighted the superiority of  $a\text{NiFc-MOFs}$  as an OER co-catalyst which could effectively boost the water oxidation activity.

To evaluate the potential practical applications, stability tests were conducted on the samples at 1.23 V vs. RHE for a duration of 3 hours (Fig. 4f). The  $\text{BiVO}_4@a\text{NiFc-MOFs}$  photoanode can maintain 87.5% of the initial photocurrent density within 3 hours. In stark contrast, both  $\text{BiVO}_4$  and  $\text{BiVO}_4@c\text{NiFc-MOFs}$  exhibit considerable photocurrent loss. Compared to the  $\text{BiVO}_4@c\text{NiFc-MOFs}$  with nanosheet embedded morphology (Fig. S2c), the higher stability of  $\text{BiVO}_4@a\text{NiFc-MOFs}$  could be attributed to the conformal coating by the core-shell structure (Fig. 1a and Fig. S2b) which prevented  $\text{V}^{5+}$  in  $\text{BiVO}_4$  lattice from dissolving into electrolyte [66]. Moreover, the existence of SMSI could facilitate the formation of V-O-Ni interfacial bonds, also effectively restraining the dissolution of  $\text{V}^{5+}$  ions from the  $\text{BiVO}_4$  lattice [67], thereby enhancing the photoelectrochemical stability. On the other hand, reconstruction of MOFs under alkaline conditions may influence the stability. Herein, the CV and in-situ Raman characterizations demonstrated that both

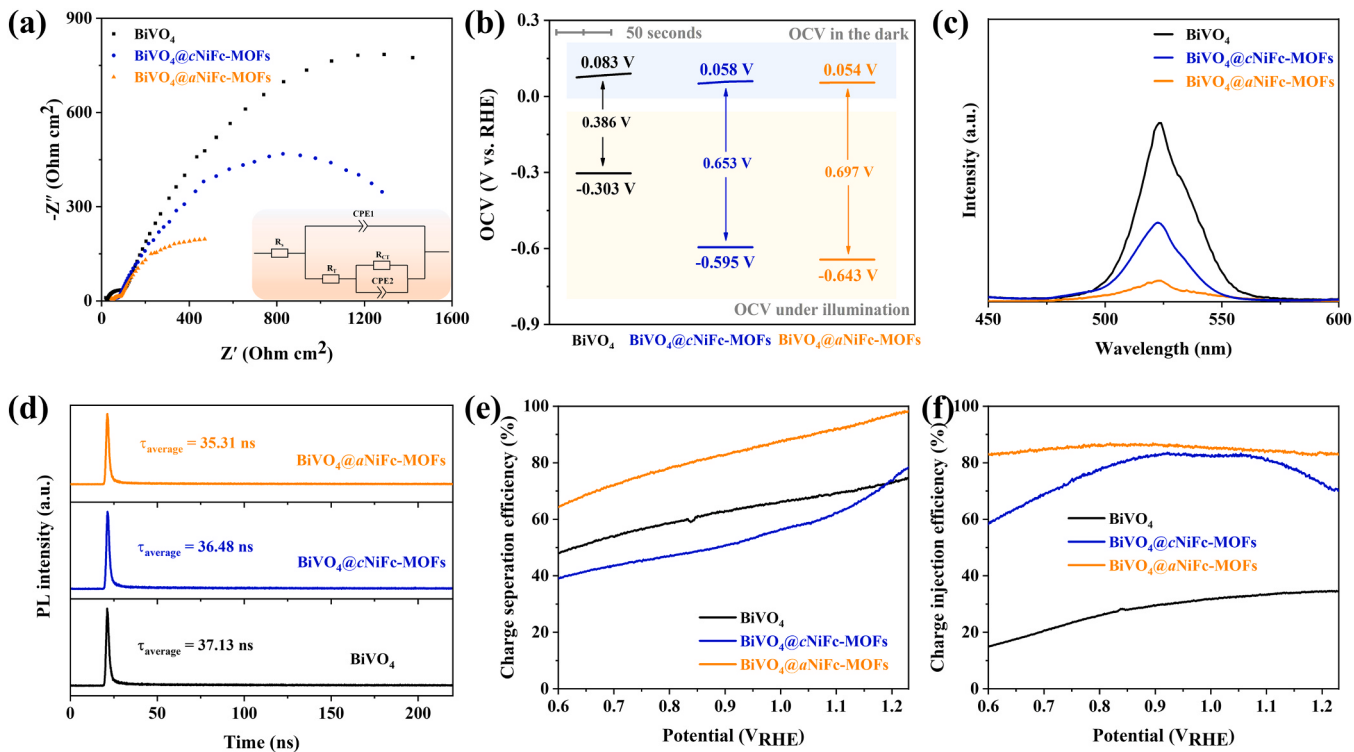


**Fig. 5.** (a) EIS Nyquist plots at 0.2 V<sub>RHE</sub> under AM 1.5 G illumination (inset is the two-RC-unit equivalent circuit). (b) OCP decay profile. (c) PL and (d) TRPL spectra of  $\text{BiVO}_4$ ,  $\text{BiVO}_4@c\text{NiFc-MOFs}$  and  $\text{BiVO}_4@a\text{NiFc-MOFs}$  photoanodes. (e)  $\eta_{\text{sep}}$  and (f)  $\eta_{\text{inj}}$  of three photoanodes.

$\text{BiVO}_4@a\text{NiFc-MOFs}$  and  $\text{BiVO}_4@c\text{NiFc-MOFs}$  photoanodes did not undergo reconstruction during PEC water splitting (Text S2, Fig. S7-8).

### 3.3. Possible mechanism analysis

To explore the underlying catalytic mechanism of the overall improved PEC performance of  $\text{BiVO}_4@a\text{NiFc-MOFs}$ , carrier kinetic and surface water oxidation kinetic were analyzed by systematic characterizations. In comparison with the  $\text{BiVO}_4$  photoanode, the UV-vis absorption spectra of the  $\text{BiVO}_4@a\text{NiFc-MOFs}$  photoanode exhibit an improved absorbance behavior with similar cut-off edges at 504 nm (Fig. S9a), corresponding to a band gap of approximately 2.49 eV (Fig. S9b). However, its light absorption capacity is slightly weaker than that of the  $\text{BiVO}_4@c\text{NiFc-MOFs}$  photoanode. Despite this, considering its superior water oxidation performance among all the samples, this unusual phenomenon precisely highlighted the unique catalytic capabilities of the  $\text{BiVO}_4@a\text{NiFc-MOFs}$  photoanode, in addition to its optical properties. Electrochemical characterizations such as M-S spectra, PEIS and open circuit potential (OCP) decay were then measured to evaluate the electronic behavior of photoanodes. The carrier density ( $N_d$ ) of  $\text{BiVO}_4@a\text{NiFc-MOFs}$  is calculated to be  $3.10 \times 10^{20} \text{ cm}^{-3}$  from the M-S spectra (Fig. S10 and Table S4), approximately 5.1 and 2.3 times higher than that of  $\text{BiVO}_4$  ( $6.09 \times 10^{19} \text{ cm}^{-3}$ ) and  $\text{BiVO}_4@c\text{NiFc-MOFs}$  ( $1.38 \times 10^{20} \text{ cm}^{-3}$ ), respectively, suggesting the robust electronic conductivity of  $\text{BiVO}_4@a\text{NiFc-MOFs}$ . This experimental result could be attributed to the increased donor density resulting from the introduction of cationic and anion vacancy defects during the amorphization of NiFc-MOFs, along with the strong metal conductivity of metallic Ni in the bulk of the  $\text{BiVO}_4@a\text{NiFc-MOFs}$  photoanode. A conventional two-RC-unit equivalent circuit (inserted in Fig. 5a) is employed to fit the Nyquist plots of PEIS (Fig. 5a). In this context,  $R_s$  typically represented a series resistance encompassing the electrolyte, external contact, and conductive substrate, while  $R_t$  denoted the bulk charge transfer resistance, and  $R_{CT}$  denoted the photoanode-electrolyte junction charge transfer resistance [68]. As outlined in Table S5, the  $R_t$  values for the

samples follow the order of  $\text{BiVO}_4@a\text{NiFc-MOFs}$  ( $112.2 \Omega$ ) <  $\text{BiVO}_4@c\text{NiFc-MOFs}$  ( $154.3 \Omega$ ) <  $\text{BiVO}_4$  ( $191.8 \Omega$ ). This sequence highlighted the central role of metallic Ni in the bulk of  $\text{BiVO}_4@a\text{NiFc-MOFs}$  in accelerating carrier migration. The metal-like state of Ni in  $a\text{NiFc-MOFs}$  established an intimate interface with the supporting semiconductor  $\text{BiVO}_4$ , resembling a heterojunction and denoting as the strong metal-support interaction. Such SMSI could significantly promote interfacial charge separation, thereby enhancing the PEC water splitting activity. Moreover, the OCP decay profile provides additional insights into interfacial charge separation (Fig. 5b). In comparison with  $\text{BiVO}_4$  and  $\text{BiVO}_4@c\text{NiFc-MOFs}$ , the  $\text{BiVO}_4@a\text{NiFc-MOFs}$  photoanode, featuring a SMSI between metallic Ni and  $\text{BiVO}_4$ , exhibits a significantly accelerated OCP decay, indicative of a larger photovoltage generation (0.697 V). This observation demonstrated that the distinctive SMSI can provide an additional driving force to promote charge separation at the interface.

Generally, PL was associated with radiative recombination, while charge separation by a junction or non-radiative recombination was responsible for quenching PL intensity and short lifetime [24]. The notably reduced PL intensity of  $\text{BiVO}_4@a\text{NiFc-MOFs}$  suggests that the introduction of  $a\text{NiFc-MOFs}$  on  $\text{BiVO}_4$  successfully enhances the interfacial hole extraction capability, thereby suppressing carrier recombination (Fig. 5c). As expected, the  $\text{BiVO}_4@a\text{NiFc-MOFs}$  photoanode with the lowest PL intensity possesses the shortest carrier lifetime (Fig. 5d and Table S6), further confirming the enhanced charge separation by SMSI through carrier dynamics on time scales. Both charge separation ( $\eta_{\text{sep}}$ ) and charge injection efficiencies ( $\eta_{\text{inj}}$ ) are calculated by using  $\text{Na}_2\text{SO}_3$  as a hole scavenger according to the Eqs. 7 and 8 (Fig. 5e, f and Fig. S11a).  $J_{\text{abs}}$  in Eq. 7 for  $\text{BiVO}_4$ ,  $\text{BiVO}_4@c\text{NiFc-MOFs}$  and  $\text{BiVO}_4@a\text{NiFc-MOFs}$  photoanodes are determined to be approximately 5.10, 5.68 and  $5.20 \text{ mA cm}^{-2}$ , respectively (Fig. S11b-d). Due to the fast kinetics for sulfite oxidation, the photogenerated holes reaching the interface between the photoanode and electrolyte would be promptly consumed. Consequently, a much high  $\eta_{\text{sep}}$  up to 98% (Fig. 5e) is achieved by  $\text{BiVO}_4@a\text{NiFc-MOFs}$  photoanode at 1.23 V<sub>RHE</sub>, indicating that almost all

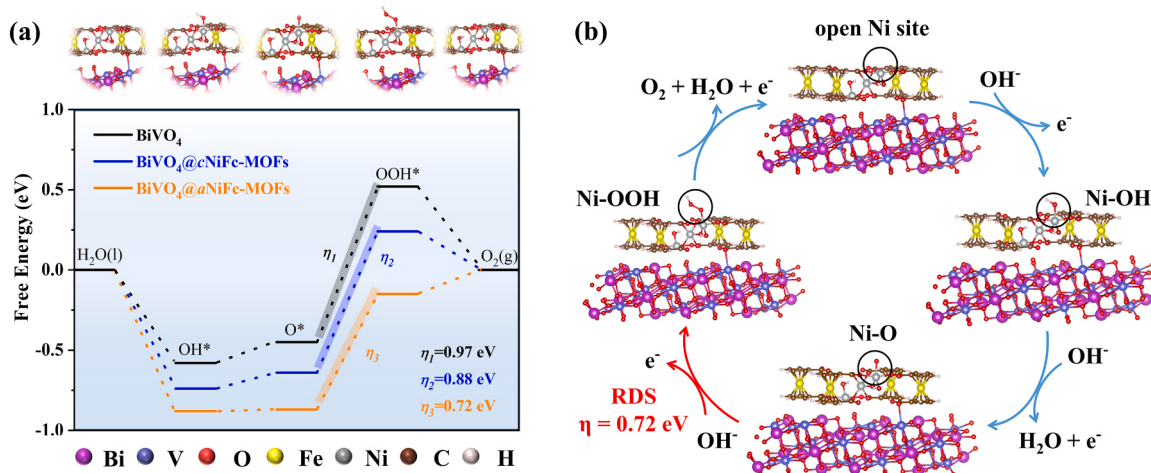


**Fig. 6.** (a) Gibbs free energy profile for OER on  $\text{BiVO}_4$ ,  $\text{BiVO}_4@c\text{NiFe-MOFs}$  and  $\text{BiVO}_4@a\text{NiFe-MOFs}$  photoanodes. (b) Different adsorption intermediates for coordinatively unsaturated Ni sites in  $\text{BiVO}_4@a\text{NiFe-MOFs}$  photoanode.

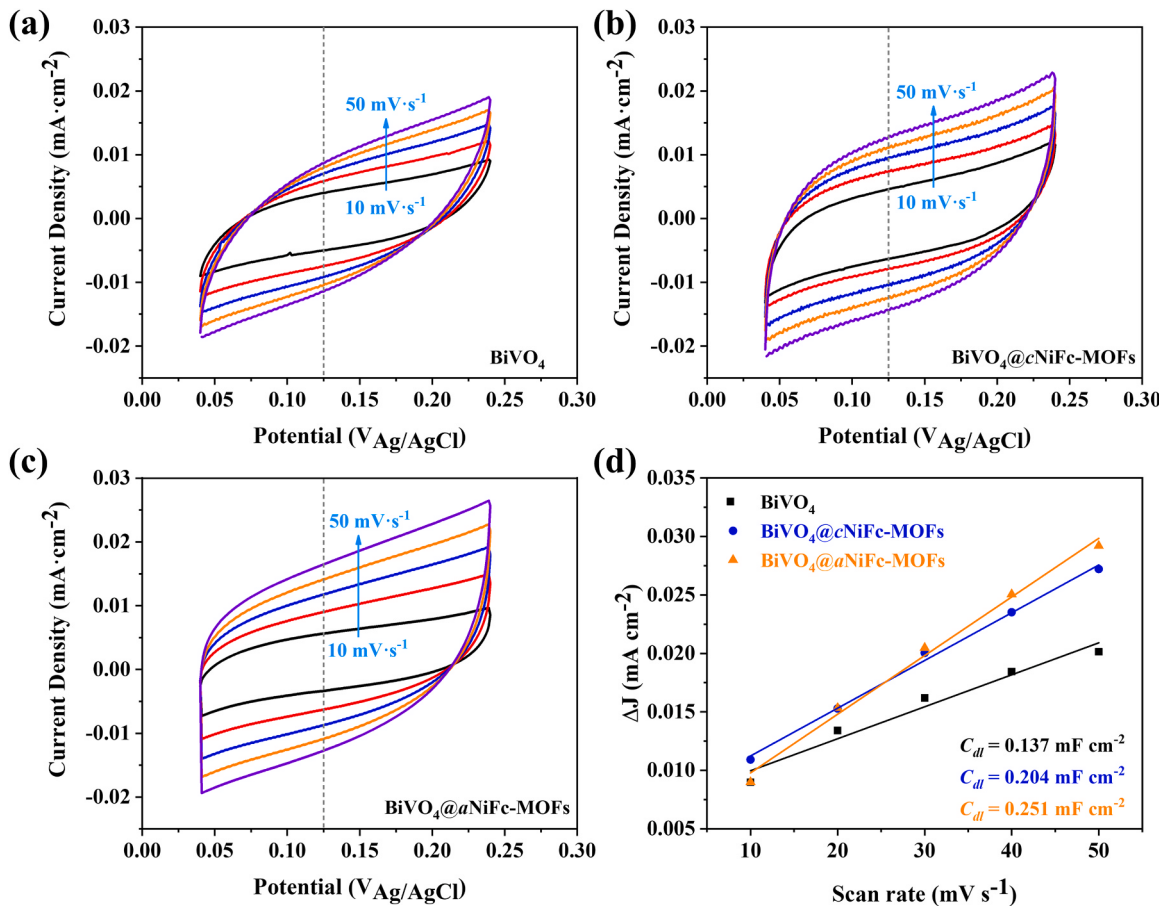


**Fig. 7.** (a)-(c) CV curves with different scan rates for  $\text{BiVO}_4$ ,  $\text{BiVO}_4@c\text{NiFe-MOFs}$  and  $\text{BiVO}_4@a\text{NiFe-MOFs}$  photoanodes. (d) Linear fitting of the CV curves.

the photogenerated carriers in bulk can be separated efficiently and transfer to electrode surface without recombination. In addition, the enhancement of the  $\eta_{inj}$  for  $\text{BiVO}_4@a\text{NiFe-MOFs}$  also demonstrates the accelerated carriers transfer dynamics (Fig. 5f).

To gain direct insights into the role of  $a\text{NiFe-MOFs}$  with abundant coordinatively unsaturated Ni sites in mediating the OER catalytic mechanism, DFT calculations were employed by constructing optimized models of  $a\text{NiFe-MOFs}$  and perfect  $c\text{NiFe-MOFs}$  on  $\text{BiVO}_4$ . The active site for the pristine  $\text{BiVO}_4$  photoanode was the V atom [69]. In contrast, the

active sites Ni were considered as adsorption sites for OER intermediates for the models of  $\text{BiVO}_4@c\text{NiFe-MOFs}$  and  $\text{BiVO}_4@a\text{NiFe-MOFs}$  photoanodes [32,37]. Following the four-electron transfer mechanism, the Gibbs free energy ( $\Delta G$ ) was calculated for each step of the OER, encompassing the adsorption of different oxygen intermediates ( $\text{OH}^*$ ,  $\text{O}^*$ ,  $\text{OOH}^*$ , and  $\text{O}_2$ ), with an additional potential ( $U = 1.23$ ) (Fig. 6a). In comparison with  $\text{BiVO}_4@c\text{NiFe-MOFs}$ , the  $\text{BiVO}_4@a\text{NiFe-MOFs}$  exhibits the lower energy barrier of the first adsorption step ( ${}^*\rightarrow\text{OH}^*$ ), which agrees well with the higher hydrophilicity with a contact angle of 52.14°

(Fig. S12). All the samples share the same rate-determining step of the conversion from  $O^*$  to  $OOH^*$ . Remarkably, the  $BiVO_4@aNiFc$ -MOFs photoanode exhibits a  $\Delta G$  of 0.72 eV for the formation of  $OOH^*$ , much lower than that of  $BiVO_4@cNiFc$ -MOFs (0.88 eV) and  $BiVO_4$  (0.97 eV) (Fig. 6a, b). In conclusion, compared with other photoanodes, the OER over the coordinatively unsaturated Ni sites of  $BiVO_4@aNiFc$ -MOF exhibited a more favorable pathway for adsorbing O adsorbates, especially for the rate-determining step of adsorbing  $^{*}OOH$ . Thus, such  $aNiFc$ -MOFs with abundant coordinatively unsaturated Ni sites on  $BiVO_4$  could thermodynamically facilitate surface water oxidation.

For further confirmation of the enhanced OER adsorption and activation behaviors, the electrochemical active surface area (ECSA) of the photoanodes was estimated through the electrochemical double layer capacitances ( $C_{dl}$ ) obtained from CV curves (Fig. 7). As anticipated,  $BiVO_4@aNiFc$ -MOFs achieves a  $C_{dl}$  of  $0.251\text{ mF cm}^{-2}$ , significantly higher than that of  $BiVO_4@cNiFc$ -MOFs ( $0.204\text{ mF cm}^{-2}$ ) and  $BiVO_4$  ( $0.137\text{ mF cm}^{-2}$ ) (Fig. 7d), indicating a substantial increase in active sites due to the exposure of coordinatively unsaturated Ni sites on the surface of  $BiVO_4@aNiFc$ -MOFs. In addition, compared with  $BiVO_4@cNiFc$ -MOFs, the  $\eta_{inj}$  of  $BiVO_4@aNiFc$ -MOFs (Fig. 5f) is higher over the potential range from 0.6 to  $1.23\text{ V}_{RHE}$ . This result suggested that more holes from the  $BiVO_4@aNiFc$ -MOFs photoanode participates in water oxidation, even under relatively low overpotential. Moreover, the dark LSV curves (Fig. S13) reveal that  $BiVO_4@aNiFc$ -MOFs exhibits an earlier onset potential and faster increase of current density compared to other photoanodes, highlighting the excellent catalytic activity of the co-catalyst  $aNiFc$ -MOFs with abundant coordinatively unsaturated Ni sites.

#### 4. Conclusion

In this study, the crystallinity of NiFc-MOFs is precisely controlled via changing the concentration of metal ions and organic linkers. The  $aNiFc$ -MOFs were successfully integrated onto the  $BiVO_4$  photoanode for PEC water splitting, which displays an outstanding photocurrent density of  $4.34\text{ mA cm}^{-2}$  at  $1.23\text{ V}_{RHE}$  with a relatively low onset potential of  $0.223\text{ V}_{RHE}$ . The subsequent structural and carrier kinetic experiments confirmed the distinctive electronic and atomic structure of the  $BiVO_4@aNiFc$ -MOFs photoanode, where the surface is the  $aNiFc$ -MOFs layer with abundant coordinatively unsaturated Ni sites and the internal Ni species adopt a metal-like state. Being attributed to the SMSI formed between the metallic Ni and  $BiVO_4$ , interfacial charge transfer and separation are significantly accelerated, resulting in great improvement of OER activity. Meanwhile, abundance of coordinatively unsaturated Ni sites on  $BiVO_4@aNiFc$ -MOFs can provide additional highly active adsorption sites for OER intermediates, creating a more favorable pathway for OER based on thermodynamics. The present work not only provide an efficient photoanode for OER, but also boost the application of  $a$ -MOFs in PEC water splitting technology.

#### CRediT authorship contribution statement

**Weihao Bai:** Conceptualization, Investigation, Methodology, Writing – original draft. **Hao Li:** Conceptualization, Investigation, Methodology, Writing – original draft. **Gang Peng:** Conceptualization, Data curation, Visualization. **Jinnan Wang:** Conceptualization, Project administration, Supervision, Writing – review & editing. **Aimin Li:** Writing – review & editing. **Philippe François-Xavier Corvini:** Visualization.

#### Declaration of Competing Interest

We have no known competing financial interests or personal relationships that could have appeared to influence the work reported in this paper.

#### Data availability

No data was used for the research described in the article.

#### Acknowledgement

This research was supported by National Natural Science Foundation of China (No. 52070095) and Jiangsu Province Water Resource Research Project (2022037).

#### Appendix A. Supporting information

Supplementary data associated with this article can be found in the online version at doi:10.1016/j.apcatb.2024.124023.

#### References

- [1] A. Fujishima, K. Honda, Electrochemical photolysis of water at a semiconductor electrode, *Nature* 238 (1972) 37.
- [2] A.J. Bard, M.A. Fox, Accounts of chemical research, *Artif. Photosynthesis - Sol. SPLITTING WATER* *Hydrog. Oxyg.* 28 (1995) 141–145.
- [3] Y. Zhang, H. Zhang, A. Liu, C. Chen, W. Song, J. Zhao, Rate-limiting O-O bond formation pathways for water oxidation on hematite photoanode, *J. Am. Chem. Soc.* 140 (2018) 3264–3269.
- [4] Z. Bai, X. Yan, Y. Li, Z. Kang, S. Cao, Y. Zhang, 3D-branched  $ZnO/CdS$  nanowire arrays for solar water splitting and the service safety research, *Adv. Energy Mater.* 6 (2016).
- [5] X. Li, S. Liu, K. Fan, Z. Liu, B. Song, J. Yu, MOF-based transparent passivation layer modified  $ZnO$  nanorod arrays for enhanced photo-electrochemical water splitting, *Adv. Energy Mater.* 8 (2018).
- [6] Y. Hu, Y. Pan, Z. Wang, T. Lin, Y. Gao, B. Luo, H. Hu, F. Fan, G. Liu, L. Wang, Lattice distortion induced internal electric field in  $TiO_2$  photoelectrode for efficient charge separation and transfer, *Nat. Commun.* 11 (2020).
- [7] G. Wang, H. Wang, Y. Ling, Y. Tang, X. Yang, R.C. Fitzmorris, C. Wang, J.Z. Zhang, Y. Li, Hydrogen-treated  $TiO_2$  nanowire arrays for photoelectrochemical water splitting, *Nano Lett.* 11 (2011) 3026–3033.
- [8] H.-J. Ahn, K.-Y. Yoon, M.-J. Kwak, J.-H. Jang, A titanium-doped  $SiO_x$  passivation layer for greatly enhanced performance of a hematite-based photoelectrochemical system, *Angew. Chem. -Int. Ed.* 55 (2016) 9922–9926.
- [9] C. Li, A. Li, Z. Luo, J. Zhang, X. Chang, Z. Huang, T. Wang, J. Gong, Surviving high-temperature calcination:  $ZrO_2$ -induced hematite nanotubes for photoelectrochemical water oxidation, *Angew. Chem. -Int. Ed.* 56 (2017) 4150–4155.
- [10] S.S. Kalanur, R. Singh, H. Seo, Enhanced solar water splitting of an ideally doped and work function tuned {002} oriented one-dimensional  $WO_3$  with nanoscale surface charge mapping insights, *Appl. Catal. B-Environ.* 295 (2021).
- [11] Y. Wang, D. Chen, J. Zhang, M.S. Balogun, P. Wang, Y. Tong, Y. Huang, Charge relays via dual carbon-actions on nanostructured  $BiVO_4$  for high performance photoelectrochemical water splitting, *Adv. Funct. Mater.* 32 (2022).
- [12] Y. Sun, H. Li, Y. Hu, J. Wang, A. Li, P.F.-X. Corvini, Single-atomic ruthenium coupling with NiFe layered double hydroxide in-situ growth on  $BiVO_4$  photoanode for boosting photoelectrochemical water splitting, *Appl. Catal. B-Environ.* 340 (2024).
- [13] L. Yao, W. Wang, T. Zhu, Y. Wang, Y. Liang, J. Fu, J. Wang, Y. Cheng, S. Liu, A rational design of  $CdS/ZnFe_2O_4/Cu_2O$  core-shell nanorod array photoanode with stair-like type-II band alignment for highly efficient bias-free visible-light-driven  $H_2$  generation, *Appl. Catal. B-Environ.* 268 (2020).
- [14] Q. Zhao, Z. Liu, Z. Guo, M. Ruan, W. Yan, The collaborative mechanism of surface S-vacancies and piezoelectric polarization for boosting  $CdS$  photoelectrochemical performance, *Chem. Eng. J.* 433 (2022).
- [15] M.A. Gaikwad, U.P. Suryawanshi, U.V. Ghorpade, J.S. Jang, M.P. Suryawanshi, J. H. Kim, Emerging surface, bulk, and interface engineering strategies on  $BiVO_4$  for photoelectrochemical water splitting, *Small* 18 (2022).
- [16] H.L. Tan, R. Amal, Y.H. Ng, Alternative strategies in improving the photocatalytic and photoelectrochemical activities of visible light-driven  $BiVO_4$ : a review, *J. Mater. Chem. A* 5 (2017) 16498–16521.
- [17] S. Wang, T. He, P. Chen, A. Du, K. Ostrikov, W. Huang, L. Wang, In situ formation of oxygen vacancies achieving near-complete charge separation in planar  $BiVO_4$  photoanodes, *Adv. Mater.* 32 (2020).
- [18] H. Yin, D. Li, X. Wang, C. Li, Surface passivation effect of ferrihydrite with hole-storage ability in water oxidation on  $BiVO_4$  photoanode, *J. Phys. Chem. C* 125 (2021) 8369–8375.
- [19] B. Pattengale, J. Ludwig, J. Huang, Atomic insight into the W-doping effect on carrier dynamics and photoelectrochemical properties of  $BiVO_4$  photoanodes, *J. Phys. Chem. C* 120 (2016) 1421–1427.
- [20] Y. Shi, Y. Yu, Y. Yu, Y. Huang, B. Zhao, B. Zhang, Boosting photoelectrochemical water oxidation activity and stability of Mo-doped  $BiVO_4$  through the uniform assembly coating of NiFe-phenolic networks, *ACS Energy Lett.* 3 (2018) 1648–1654.
- [21] K.-H. Ye, H. Li, D. Huang, S. Xiao, W. Qiu, M. Li, Y. Hu, W. Mai, H. Ji, S. Yang, Enhancing photoelectrochemical water splitting by combining work function tuning and heterojunction engineering, *Nat. Commun.* 10 (2019).

- [22] Y. Zhang, X. Chen, F. Jiang, Y. Bu, J.-P. Ao, BiVO<sub>4</sub> photoanode modification by in-doping and anoxic annealing by synergistic regulation, *Acs Sustain. Chem. Eng.* 8 (2020) 9184–9194.
- [23] R.-T. Gao, D. He, L. Wu, K. Hu, X. Liu, Y. Su, L. Wang, Towards long-term photostability of nickel hydroxide/BiVO<sub>4</sub> photoanodes for oxygen evolution catalysts via *in situ* catalyst tuning, *Angew. Chem. -Int. Ed.* 59 (2020) 6213–6218.
- [24] S. Liu, R.-T. Gao, R. Zhang, Z. Wang, X. Liu, T. Nakajima, X. Zhang, Y. Su, L. Wang, Tungsten induced defects control on BiVO<sub>4</sub> photoanodes for enhanced solar water splitting performance and photocorrosion resistance, *Appl. Catal. B-Environ.* 298 (2021).
- [25] T. Eo, T. Katsuki, M.R. Berber, Z.N. Zahran, E.A. Mohamed, Y. Tsubonouchi, A. M. Alenad, N.A. Althubiti, M. Yagi, Handy protocol of nitrogen-doped BiVO<sub>4</sub> photoanode for visible light-driven water oxidation, *Acs Appl. Energy Mater.* 4 (2021) 2983–2989.
- [26] W. Bai, Y. Zhou, G. Peng, J. Wang, A. Li, P.F.-X. Corvini, Engineering efficient hole transport layer Ferrihydrite-MXene on BiVO<sub>4</sub> photoanodes for photoelectrochemical water splitting: work function and conductivity regulated, *Appl. Catal. B-Environ.* (2022) 315.
- [27] T. Reier, M. Oezaslan, P. Strasser, Electrocatalytic oxygen evolution reaction (OER) on Ru, Ir, and Pt catalysts: a comparative study of nanoparticles and bulk materials, *Acs Catal.* 2 (2012) 1765–1772.
- [28] W. Cheng, X. Zhao, H. Su, F. Tang, W. Che, H. Zhang, Q. Liu, Lattice-strained metal-organic framework arrays for bifunctional oxygen electrocatalysis, *Nat. Energy* 4 (2019) 115–122.
- [29] Z. Xue, K. Liu, Q. Liu, Y. Li, M. Li, C.-Y. Su, N. Ogiwara, H. Kobayashi, H. Kitagawa, M. Liu, G. Li, Missing-linker metal-organic frameworks for oxygen evolution reaction, *Nat. Commun.* 10 (2019).
- [30] C. Zhang, Q. Qi, Y. Mei, J. Hu, M. Sun, Y. Zhang, B. Huang, L. Zhang, S. Yang, Rationally reconstructed metal-organic frameworks as Robust oxygen evolution electrocatalysts, *Adv. Mater.* 35 (2023).
- [31] Y. Li, Y. Guo, D. Luan, X. Gu, X.W. Lou, An unlocked two-dimensional conductive Zn-MOF on polymeric carbon nitride for photocatalytic H<sub>2</sub>O<sub>2</sub> production, *Angew. Chem. -Int. Ed.* 62 (2023).
- [32] J. Liang, X. Gao, B. Guo, Y. Ding, J. Yan, Z. Guo, E.C.M. Tse, J. Liu, Ferrocene-based metal-organic framework nanosheets as a Robust oxygen evolution catalyst, *Angew. Chem. -Int. Ed.* 60 (2021) 12770–12774.
- [33] Y. Liu, Y. Liu, B. Li, X. Guo, J. Zhang, G. Zhu, Activation of ferrocene-based coordination compounds for oxygen evolution and the application in zinc-air battery, *J. Alloy. Compd.* 967 (2023).
- [34] G. Givaja, P. Amo-Ochoa, C.J. Gomez-Garcia, F. Zamora, Electrical conductive coordination polymers, *Chem. Soc. Rev.* 41 (2012) 115–147.
- [35] H.-N. Wang, X. Meng, L.-Z. Dong, Y. Chen, S.-L. Li, Y.-Q. Lan, Coordination polymer-based conductive materials: ionic conductivity vs. electronic conductivity, *J. Mater. Chem. A* 7 (2019) 24059–24091.
- [36] J. Hu, Q. Xu, X. Wang, X. Huang, C. Zhou, Y. Ye, L. Zhang, H. Pang, Charge-transfer-regulated bimetal ferrocene-based organic frameworks for promoting electrocatalytic oxygen evolution, *Carbon Energy* 5 (2023).
- [37] J. Ding, D. Guo, N. Wang, H.-F. Wang, X. Yang, K. Shen, L. Chen, Y. Li, Defect engineered metal-organic framework with accelerated structural transformation for efficient oxygen evolution reaction, *Angew. Chem. -Int. Ed.* 62 (2023).
- [38] Y. Tan, C. Lin, X. He, J. Zou, C. Yan, J. Tian, Introducing a synergistic ligand containing an exotic metal in metal-organic framework nanoarrays enabling superior electrocatalytic water oxidation performance, *Inorg. Chem.* 61 (2022) 11432–11441.
- [39] T.D. Bennett, S. Horike, Liquid, glass and amorphous solid states of coordination polymers and metal-organic frameworks, *Nat. Rev. Mater.* 3 (2018) 431–440.
- [40] C. Liu, J. Wang, J. Wan, Y. Cheng, R. Huang, C. Zhang, W. Hu, G. Wei, C. Yu, Amorphous Metal-organic framework-dominated nanocomposites with both compositional and structural heterogeneity for oxygen evolution, *Angew. Chem. -Int. Ed.* 59 (2020) 3630–3637.
- [41] S. Anantharaj, S. Noda, Amorphous catalysts and electrochemical water splitting: an untold story of harmony, *Small* 16 (2020).
- [42] J. Fonseca, T. Gong, L. Jiao, H.-L. Jiang, Metal-organic frameworks (MOFs) beyond crystallinity: amorphous MOFs, MOF liquids and MOF glasses, *J. Mater. Chem. A* 9 (2021) 10562–10611.
- [43] T.W. Kim, K.-S. Choi, Nanoporous BiVO<sub>4</sub> photoanodes with dual-layer oxygen evolution catalysts for solar water splitting, *Science* 343 (2014) 990–994.
- [44] Z. Luo, C. Li, S. Liu, T. Wang, J. Gong, Gradient doping of phosphorus in Fe<sub>2</sub>O<sub>3</sub> nanoarray photoanodes for enhanced charge separation, *Chem. Sci.* 8 (2017) 91–100.
- [45] Z.-Y. Wang, H.-M. Li, S.-S. Yi, M.-Z. You, H.-J. Jing, X.-Z. Yue, Z.-T. Zhang, D.-L. Chen, In-situ coating of multifunctional FeCo-bimetal organic framework nanolayers on hematite photoanode for superior oxygen evolution, *Appl. Catal. B-Environ.* 297 (2021).
- [46] S.-S. Yi, Z.-Y. Wang, H.-M. Li, Z. Zafar, Z.-T. Zhang, L.-Y. Zhang, D.-L. Chen, Z.-Y. Liu, X.-Z. Yue, Coupling effects of indium oxide layer on hematite enabling efficient photoelectrochemical water splitting, *Appl. Catal. B-Environ.* 283 (2021).
- [47] Z. Wang, X. Mao, P. Chen, M. Xiao, S.A. Monny, S. Wang, M. Konarova, A. Du, L. Wang, Understanding the roles of oxygen vacancies in hematite-based photoelectrochemical processes, *Angew. Chem. -Int. Ed.* 58 (2019) 1030–1034.
- [48] X. Chang, T. Wang, P. Zhang, J. Zhang, A. Li, J. Gong, Enhanced surface reaction kinetics and charge separation of p-n heterojunction Co<sub>3</sub>O<sub>4</sub>/BiVO<sub>4</sub> photoanodes, *J. Am. Chem. Soc.* 137 (2015) 8356–8359.
- [49] J.B. Liu, H. Wang, S. Wang, H. Yan, Hydrothermal preparation of BiVO<sub>4</sub> powders, *Mater. Sci. Eng. B-Solid State Mater. Adv. Technol.* 104 (2003) 36–39.
- [50] J.-B. Pan, B.-H. Wang, J.-B. Wang, H.-Z. Ding, W. Zhou, X. Liu, J.-R. Zhang, S. Shen, J.-K. Guo, L. Chen, C.-T. Au, L.-L. Jiang, S.-F. Yin, Activity and stability boosting of an oxygen-vacancy-rich BiVO<sub>4</sub> photoanode by NiFe-MOFs thin layer for water oxidation, *Angew. Chem. -Int. Ed.* 60 (2021) 1433–1440.
- [51] R. Lin, S.-M. Bak, Y. Shin, R. Zhang, C. Wang, K. Kisslinger, M. Ge, X. Huang, Z. Shadik, A. Pattammattel, H. Yan, Y. Chu, J. Wu, W. Yang, M.S. Whittingham, H. L. Xin, X.-Q. Yang, Hierarchical nickel valence gradient stabilizes high-nickel content layered cathode materials, *Nat. Commun.* 12 (2021).
- [52] H. Huang, G. Yu, X. Zhao, B. Cui, J. Yu, C. Zhao, H. Liu, X. Li, Atomic Ni directional-substitution on ZnIn<sub>2</sub>S<sub>4</sub> nanosheet to achieve the equilibrium of elevated redox capacity and efficient carrier-kinetics performance in photocatalysis, *J. Energy Chem.* 88 (2024) 272–281.
- [53] Z. Zhou, Y. Kong, H. Tan, Q. Huang, C. Wang, Z. Pei, H. Wang, Y. Liu, Y. Wang, S. Li, X. Liao, W. Yan, S. Zhao, Cation-vacancy-enriched nickel phosphide for efficient electrosynthesis of hydrogen peroxides, *Adv. Mater.* 34 (2022).
- [54] G. Dong, M. Hong, C.Y. Duan, L. Feng, Q.J. Meng, Novel ferrocene-based mixed-metal coordination polymers, *J. Chem. Soc. -Dalton Trans.* (2002) 2593–2594.
- [55] Y. Qi, B. Zhang, G. Zhang, Z. Zheng, T. Xie, S. Chen, G. Ma, C. Li, K. Domen, F. Zhang, Efficient overall water splitting of a suspended photocatalyst boosted by metal-support interaction, *Joule* 8 (2024) 193–203.
- [56] D. Chen, Z. Xie, Y. Tong, Y. Huang, Review on BiVO<sub>4</sub>-based photoanodes for photoelectrochemical water oxidation: the main influencing factors, *Energy Fuels* 36 (2022) 9932–9949.
- [57] K. Zhang, B. Jin, C. Park, Y. Cho, X. Song, X. Shi, S. Zhang, W. Kim, H. Zeng, J. H. Park, Black phosphorene as a hole extraction layer boosting solar water splitting of oxygen evolution catalysts, *Nat. Commun.* 10 (2019).
- [58] S. Zhou, K. Chen, J. Huang, L. Wang, M. Zhang, B. Bai, H. Liu, Q. Wang, Preparation of heterometallic CoNi-MOFs-modified BiVO<sub>4</sub>: a steady photoanode for improved performance in photoelectrochemical water splitting, *Appl. Catal. B-Environ.* (2020) 266.
- [59] F.F. Abdi, R. van de Krol, Nature and light dependence of bulk recombination in Co-Pi-catalyzed BiVO<sub>4</sub> photoanodes, *J. Phys. Chem. C* 116 (2012) 9398–9404.
- [60] B. Zhang, L. Wang, Y. Zhang, Y. Ding, Y. Bi, Ultrathin FeOOH nanolayers with abundant oxygen vacancies on BiVO<sub>4</sub> photoanodes for efficient water oxidation, *Angew. Chem. -Int. Ed.* 57 (2018) 2248–2252.
- [61] H. Luo, C. Liu, Y. Xu, C. Zhang, W. Wang, Z. Chen, An ultra-thin NiOOH layer loading on BiVO<sub>4</sub> photoanode for highly efficient photoelectrochemical water oxidation, *Int. J. Hydrog. Energy* 44 (2019) 30160–30170.
- [62] Y. Peng, G.V. Govindaraju, D.K. Lee, K.-S. Choi, T.L. Andrew, Integrating a semitransparent, fullerene-free organic solar cell in tandem with a BiVO<sub>4</sub> photoanode for unassisted solar water splitting, *Acs Appl. Mater. Interfaces* 9 (2017) 22449–22455.
- [63] P. Yue, H. She, L. Zhang, B. Niu, R. Lian, J. Huang, L. Wang, Q. Wang, Super-hydrophilic CoAl-LDH on BiVO<sub>4</sub> for enhanced photoelectrochemical water oxidation activity, *Appl. Catal. B-Environ.* 286 (2021).
- [64] H. She, P. Yue, X. Ma, J. Huang, L. Wang, Q. Wang, Fabrication of BiVO<sub>4</sub> photoanode cocatalyzed with NiCo-layered double hydroxide for enhanced photoactivity of water oxidation, *Appl. Catal. B-Environ.* 263 (2020).
- [65] X. Lei, Q. Tang, Y. Zheng, P. Kidkhunthod, X. Zhou, B. Ji, Y. Tang, High-entropy single-atom activated carbon catalysts for sustainable oxygen electrocatalysis, *Nat. Sustain.* 6 (2023) 816–826.
- [66] D.K. Lee, K.-S. Choi, Enhancing long-term photostability of BiVO<sub>4</sub> photoanodes for solar water splitting by tuning electrolyte composition, *Nat. Energy* 3 (2018) 53–60.
- [67] B. Zhang, X. Huang, Y. Zhang, G. Lu, L. Chou, Y. Bi, Unveiling the activity and stability origin of BiVO<sub>4</sub> photoanodes with FeNi oxyhydroxides for oxygen evolution, *Angew. Chem. -Int. Ed.* 59 (2020) 18990–18995.
- [68] H. Zhang, D. Li, W.J. Byun, X. Wang, T.J. Shin, H.Y. Jeong, H. Han, C. Li, J.S. Lee, Gradient tantalum-doped hematite homojunction photoanode improves both photocurrents and turn-on voltage for solar water splitting, *Nat. Commun.* 11 (2020).
- [69] S. Jin, X. Ma, J. Pan, C. Zhu, S.E. Saji, J. Hu, X. Xu, L. Sun, Z. Yin, Oxygen vacancies activating surface reactivity to favor charge separation and transfer in nanoporous BiVO<sub>4</sub> photoanodes, *Appl. Catal. B-Environ.* 281 (2021).